# Insights into Electrochemical Sodium Metal Deposition as Probed with *in Situ* ^{23}Na NMR

Paul M. Bayley, Nicole M. Trease, and Clare P. Grey*

Department of Chemistry, University of Cambridge, Lensfield Road, Cambridge, U.K. CB2 1EW

Ⓢ *Supporting Information*

ABSTRACT: Sodium batteries have seen a resurgence of interest from researchers in recent years, owing to numerous favorable properties including cost and abundance. Here we examine the feasibility of studying this battery chemistry with *in situ* NMR, focusing on Na metal anodes. Quantification of the NMR signal indicates that Na metal deposits with a morphology associated with an extremely high surface area, the deposits continually accumulating, even in the case of galvanostatic cycling. Two regimes for the electrochemical cycling of Na metal are apparent that have implications for the use of Na anodes: at low currents, the Na deposits are partially removed on reversing the current, while at high currents, there is essentially no removal of the deposits in the initial stages. At longer times, high currents show a significantly greater accumulation of deposits during cycling, again indicating a much lower efficiency of removal of these structures when the current is reversed.
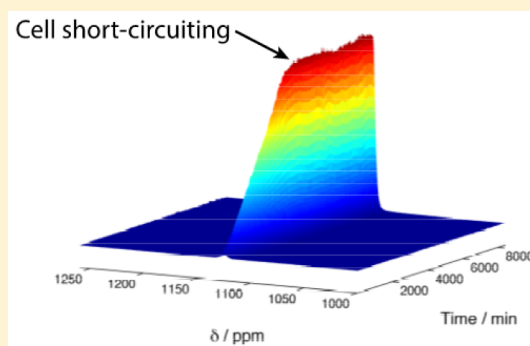
INTRODUCTION

As the demand for batteries continuously increases, research aimed at advancing existing technology should be coupled with the investigation of alternative chemistries, so as to provide the required high energy density and low cost sought by industry and consumers. Although lithium battery technology offers the highest attainable volumetric and gravimetric energy density, its increased use is expected to further drive up costs and exclude its widespread deployment in certain applications (e.g., grid storage).[1] Thus, the investigation of alternative chemistries that make use of the significantly more abundant sodium is necessary. Sodium ion batteries (NIBs) are an attractive alternative to Li due to a number of factors including a reasonable operating voltage (−2.71 V vs SHE for the Na$^+$|Na couple), comparable cathodes to those used in Li-ion technology, lower costs and greater natural abundance compared to Li, and the ability to replace the costly Cu negative current collector with Al.

The highest capacity anodes can, in principle, be achieved by using a metal electrode. However, for Li-ion batteries, commercial adoption of Li metal anodes for secondary batteries has been hindered by the dendritic morphology of the electrodeposited metal formed during charging. High-surface-area (HSA) mossy and dendritic structures are formed that can penetrate the separator, resulting in short circuits that may lead to thermal runaway and fire or explosion, presenting an unacceptable risk. There are a wide range of studies on the formation and growth of Li dendrites, both *in situ* and *ex situ*,[2−6] and a variety of theoretical models have been developed that further our understanding of this phenomenon and formulate approaches to suppress the dendrites. Although

there has recently been a resurgence of interest in this topic by numerous researchers, a thorough understanding of the mechanisms of dendrite formation and growth remains elusive. Such models include the Barton and Bockris[7] model that defines a critical overpotential for dendrite initiation and describes a change in the diffusion field around dendrites that promotes tip-based growth. Theoretical diffusion-limited aggregation[8] models have been used in Monte Carlo simulations to study aggregation that describes dendritic growth, which afford great scope at studying the influence of parameters such as surface tension, kinetics, and size dispersion of nuclei.[9] The model by Chazalviel et al.[10,11] defines a critical current density for dendrite initiation based on the concentration of anions at the electrode surface falling to zero. This model has recently shown encouraging correlation with Li symmetrical cells studied using magnetic resonance imaging (MRI).[12] The investigation of electrodeposited Na metal, the most analogous system to Li, represents a suitable alternative to gain further insights into the formation of HSA microstructures during the electrodeposition of alkali metals in general. Metallic Na anodes, in their own right, provide high capacity (1166 mAh g^{-1}) and were the first commercially adopted electrode materials (albeit in the molten state) for NIBs. Although safety concerns with Na metal have driven the search for alternative anodes, difficult challenges still remain for all of these anodes to allow successful incorporation into full cells including the formation of an effective passivation layer of the electrode that will survive the larger volume changes inherent to, for example,

alloy chemistry.[13] The study of Na metal anodes is therefore of relevance to primary and next-generation secondary NIBs. To date, there have been no detailed systematic investigations of dendrite formation in these systems. Furthermore, this study establishes a methodology that can be used to investigate Na deposition on other electrode systems (such as the nucleation and growth of metallic Na on hard carbon surfaces, hard carbons currently representing the most common Na anode materials[13]).

In situ nuclear magnetic resonance (NMR) spectroscopy of electrochemical devices has been shown to be a unique and indispensable tool for the nondestructive analysis of batteries,[4,14] supercapacitors,[15] and fuel cells.[16] In studies of Li microstructure (dendrites, moss, etc.), such a tool gives valuable and quantitative insight, with adequate temporal resolution, into the formation and growth of microstructural Li metal even before it becomes apparent in the electrochemistry.[4] The approach makes use of the exponential decay of the radio frequency (RF) field as it penetrates into the bulk metal anode. This is quantified via the skin depth, which is defined by the depth at which the RF field falls to $1/e$ (~37%) of that at the surface (12.3 μm in these experiments). The key to these experiments is that the deposited microstructures are typically much smaller than the skin depth and are penetrated fully by the RF, whereas the bulk metal experiences skin depth effects, and thus is not fully detected in the NMR signal (i.e., only the surface of the bulk metal is detected). Thus, an increase in signal intensity during the *in situ* experiment is directly attributed to microstructural growth and is a quantifiable measure of the amount of metal microstructures deposited; see the Supporting Information for further details.

■ EXPERIMENTAL SECTION

The electrolyte and bag cells were all prepared in an Ar glovebox (H_2O and O_2 <0.1 ppm). Propylene carbonate (PC, 99.9%, 50 ppm of H_2O, Aldrich) was used as received. Na bis(trifluoromethylsulfonyl)imide (NaTFSI) was synthesized by reacting excess Na hydrogen carbonate (Breckland Scientific) with hydrogen bis(trifluoromethylsulfonyl)-imide (>99%, Iolitec) in H_2O. After drying *in vacuo* for 24 h, the remaining salts were mixed with dry acetonitrile (<50 ppm, H_2O by Metrohm 899 Karl Fischer Coulometer) and filtered twice with 0.2 μm cellulose syringe filters. The acetonitrile was then removed *in vacuo* leaving the white NaTFSI product (yield >99%) that was dried a further 48 h at 100 °C prior to use. The electrolyte used throughout this work is 1 M NaTFSI in PC.

Symmetrical Na metal bag cells were assembled with copper mesh current collectors and freshly prepared Na (of dimension $10 \times 5 \times 0.5$ mm) cut from cubes (Aldrich, 99.9%), as described elsewhere for Li cells.[4] All NMR measurements were performed on an Oxford Instruments wide-bore magnet operating at 7.04 T with a Tecmag LapNMR console and a Bruker X static probe tuned to ^{23}Na (79.353 MHz). *In situ* spectra were acquired using a Hahn-echo pulse sequence; τ_{echo} = 30 μs, $\pi/2$ = 8 μs, and a recycle delay of 1 s ($\gg 5T_1$ to limit RF heating). Spectra are referenced to 1 M NaCl at 0 ppm. *In situ* NMR electrochemical measurements were performed using a Biologic VSP potentiostat, with either continuous galvanostatic (constant current) plating or galvanostatic cycling (84 min per half cycle) applied to the cells. Chronoamperometry and cyclic voltammetry (CV) were performed using a Biologic SP-100 potentiostat connected to three electrode cells using Na electrodes (except in the case of CV where a Pt wire working electrode was utilized) inside an Ar-filled glovebox. These cells are based on the bag cell design ($10 \times 5 \times 0.5$ mm electrodes), ~0.5 mL of electrolyte, with a small ($2 \times 5 \times 0.5$ mm) reference electrode. All measurements are performed at room temperature (293 K).

Diffusion measurements were performed at 293 K on a Bruker 300 AvanceIII spectrometer fitted with a Diff50 z-gradient diffusion probe using a 5 mm RF coil and NMR tube. Applying the stimulated echo pulse sequence to minimize T_2 losses, a total of 16 gradient steps were acquired with either 16 or 1024 transients (for ^{19}F and ^{23}Na, respectively); the data were then fit to the Stejskal–Tanner equation. The fast relaxation of ^{23}Na (T_1 = 2.4 ms) required a compromise in the gradient pulses applied during the diffusion experiment, introducing considerable error (at least 20% in this case) into the measurements, because of the significant time for the gradient pulses (δ = 0.5 ms, 100 μs rise time, maximum 800 G cm^{-1}) in relation to the diffusion time (Δ = 5 ms) and other gradient pulse effects on signal attenuation.[17] To determine if these parameters were reliable, we obtained the diffusion coefficient for 0.1 M NaCl that had previously been published in the literature as 1.12×10^{-9} m^2 s^{-1} at 298 K.[18] In this work we measure 2×10^{-9} m^2 s^{-1}, indicating that although reasonable error is introduced due to the nonoptimum parameters, we still retain a reasonable estimate. Experiments on ^{19}F were performed using δ = 1 ms and Δ = 20 ms.

■ RESULTS AND DISCUSSION

Figure 1 shows the ^{23}Na spectrum of a symmetrical bag cell, while the inset shows the influence of the orientation of the
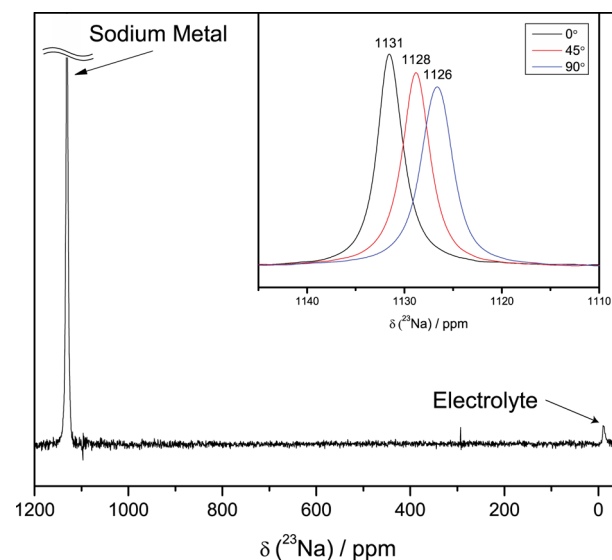

Figure 1. ^{23}Na NMR spectrum of Na symmetrical bag cell and (inset) the orientation dependence of the Na metal electrode with respect to the main external magnetic field (B_0).

metal electrode with respect to the static magnetic field (B_0). The Na$^+$ ions in the electrolyte are visible at −10 ppm, and the Na metal signal is observed at a much higher frequency of around 1130 ppm due to the Knight shift caused by the temperature-independent paramagnetism (TIP) of the free electrons. The larger Knight shift of Na compared to Li (250−270 ppm, depending on orientation to B_0) is primarily due to the larger atomic volume and density of states at the Fermi level, continually increasing down the alkali metal series (although other contributions become more significant for the larger atoms).[19] Similar to the *in situ* ^{7}Li NMR of Li metal electrodes,[20] the bulk magnetic susceptibility (BMS) effect, caused by the TIP properties of a metal, and the flat anisotropic shape of the bag cells, results in shifts in the NMR resonances as a function of the bag orientation with respect to B_0. This orientation-dependent shift is much smaller for Na than Li metal (~5 ppm vs ~30), at least in part due to the smaller

susceptibility of Na vs Li (a factor of ∼0.6 smaller[21]). The apparent [23]Na intensity variation between the orientations is the result of broadening of the signal, the integrated intensity remaining constant.

Symmetrical Na cells (i.e., cells with two essentially identical Na metal electrodes) were either galvanostatically plated or cycled (i.e., either constant current deposition (plating) or constant current deposition and stripping) at a variety of low-to-reasonably high current densities until failure, while continuously acquiring the ^{23}Na NMR spectra of the metal. Although there is potentially useful information that can be derived from the diamagnetic [23]Na signal of the electrolyte, such as solid electrolyte interphase (SEI) components and Na$^+$ concentration of the electrolyte, the frequency separation between this signal and that of the large Knight shifted Na metal signal exceeds the excitation bandwidth of the experiment, and it is difficult to acquire quantifiable spectra of both species simultaneously with the setup used here.

Examples of the electrochemistry of two cells, one continually plated and the other cycled, both at current densities of 1 mA cm^{-2} (Figure 2), initially display a constant
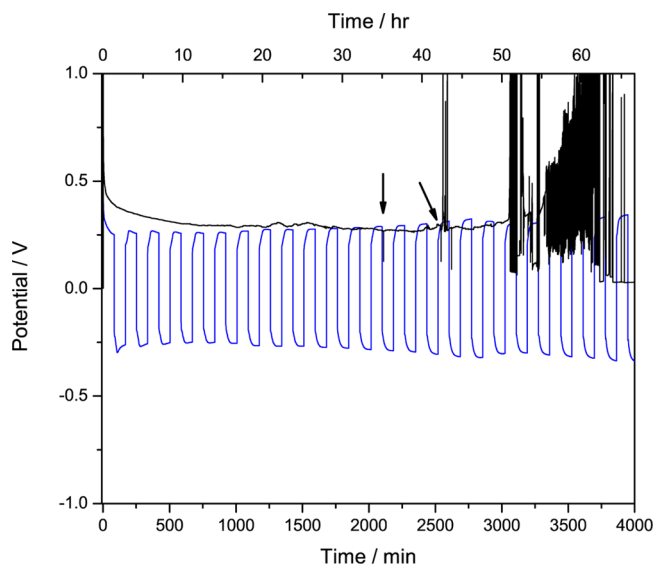
Figure 2. Electrochemistry of Na symmetrical bag cells during galvanostatic plating (black curve) and cycling (blue curve; current flow reversed every 84 min) at 1 mA cm^{-2}. Arrows indicate the initial short circuits observed during plating (black curve). The voltage is truncated at 1 V for clarity.

overpotential (of approximately ±0.3 V), indicating the formation of a stable SEI on the Na deposits. The complete set of in situ electrochemical data is provided in the Supporting Information. In the case of the continually plated cell shown in Figure 2, short-circuiting behavior begins at around 2100 min (indicated by the arrows in Figure 2). The cell continues to operate, the overpotential returning to ±0.3 V, likely because the small dendritic short circuits briefly carry the whole current of the cell and break contact because of joule heating and melting. This is reminiscent of the fuse mechanism previously described by Rosso et al.[22] for Li dendrites. Welding events are not, however, observed. These have been observed for Li metal anodes and occur when a highly intertwined network of dendrites (coated in an insulating SEI) connects to the opposite electrode (forming a short circuit). Rapid current flow through the short circuit not only breaks the electrical

connection (via a fusing mechanism) but also results in welding (rationalized by the dc Branly effect[23]) and the formation of a single, thicker metallic structure, which reduces the overpotential. Such a welding event would cause a consistently lower overpotential after the short-circuiting behavior. This is not observed in any of the electrochemical data (in Figure 2 and the Supporting Information), the short-circuiting events instead being associated with spikes. This suggests that the Na microstructures do not comprise a highly intertwined network/morphology, a key prerequisite to generate this effect. It should also be noted that large positive spikes in potential are also observed following the appearance of short-circuiting behavior. Although the exact origin of this potential instability is unknown, it presumably relates to the formation of different SEI species on the electrode surface.

The [23]Na metal signal grows continuously throughout the in situ NMR electrochemical experiments (Figure S2 in the Supporting Information), during both plating and cycling, for all currents investigated. This indicates that at least part of the deposited Na does not experience skin depth limitations. Microstructures are formed that are more effectively excited by the RF than the initial smooth anode electrode. Only very small changes to the line shape of the [23]Na metal signal were observed in this study (Figure S1). This is in contrast to the Li−metal system where a well-resolved second signal is observed for both cycling and galvanostatic plating, which is attributed to microstructural growth perpendicular to the metal surface.[4] In the [23]Na system, only a growth of a slight shoulder is evident in the initial stages, which we similarly ascribe to the formation of microstructures perpendicular to the plane of the electrode (Figure S1). The poorer resolution in this system, at least in the magnetic field studied here, is attributed to the smaller susceptibility and thus smaller BMS shift (5 ppm) of Na metal. In the Li studies, deconvolution of the second signal yielded quantifiable information on the amount and type of microstructures.[14,24] In this study, attempts to deconvolute the spectra based on two or more resonances yielded unreliable results due to the much smaller BMS shift, making it difficult to distinguish between different types of Na metal morphologies. Note that the overall intensity change is still a measure of the amount of microstructure formation. We now explore this in more detail.

Cells were continuously galvanostatically plated at 0.5, 1, and 2 mA cm^{-2} (Figure 3A), and the integral of the [23]Na metal resonance was compared to cells galvanostatically cycled at the same current densities (Figure 3B) to determine the efficiency of removal of any deposited microstructures. The full electrochemistry of these cells is shown in Figures S3−S5. These data are normalized to unity for the pristine Na electrodes, showing that the absolute amount of metallic ^{23}Na detected by the NMR experiment under all electrochemical conditions increases continuously. All samples initially exhibit a linear dependence of the amount of Na metal detected by the NMR experiment with respect to time. The slope observed for Na metal deposition doubles concomitantly with the current density, suggesting the origin of the change is a direct result of the electrochemistry. The cell has technically failed beyond the linear region of these data, presumably because the development of a large overpotential (spiking up to 4.59 V vs Na|Na$^+$) causes passivation of the electrode due to electrolyte breakdown, preventing further deposition of Na metal. Previous work has shown the development of an oxidative current in this electrolyte system with an onset potential of 3.3 V vs Na|Na$^+$.[25]
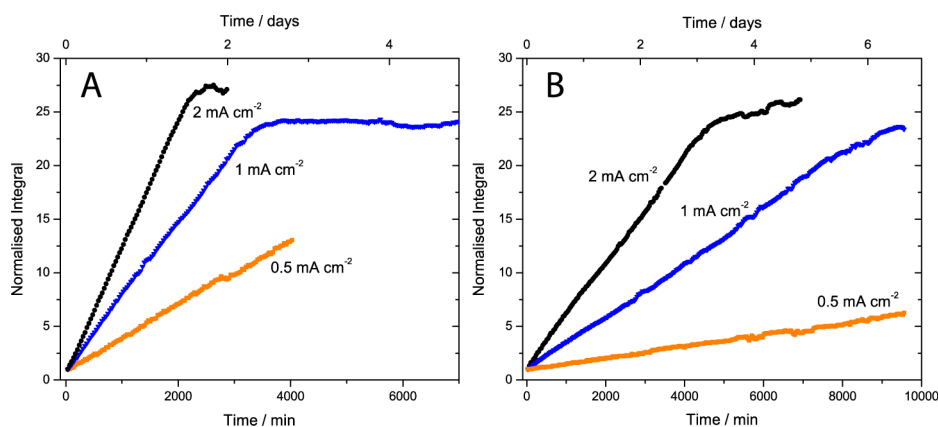
Figure 3. Integral of the normalized ^{23}Na metal resonance for (A) continuous galvanostatic deposition and (B) galvanostatic cycling at three different current densities.

This is most clearly seen for the cell continuously plated at 1 mA cm^{-2} (Figure 3A) that was measured well after the large overpotential developed at 3000 min (see Figure 2). Comparison of the continuously plated and cycled cells at the same current density (Figure 3A,B) clearly shows that cycling reduces the accumulation of Na metal, indicating that some of the HSA deposits are removed following the reversal of the current. However, microstructures do accumulate during the cycling experiments, since the NMR signal intensity continues to grow.

To extract further information from the experimental data, quantification of the NMR signal from the electrodes within the context of the skin depth is required. In this work, we apply the approach of Chandrashekar et al.[26] to Na metal as described in the Supporting Information. In short, the RF can be considered to excite a volume per unit surface area of the bulk electrode that can be quantified by integrating the RF field strength with respect to the skin depth. The ratio of the detected signal to volume (i.e., mass) of the bulk electrode is then used to calculate the mass of Na deposited (m_{NMR}) from the increased signal intensity. A reasonable correlation is obtained between the calculated mass of Na deposited from Faraday's law (m_{eChem}) and the NMR spectra, shown in Figure 4, for the continuously plated samples using this approach. If the RF field fails to penetrate through the Na microstructures to the microstructures near the bulk electrode or to the bulk electrode itself, then $m_{NMR} < m_{eChem}$. As the NMR is detecting the Na metal from both electrodes, it is likely that this overestimation in these calculations is at least, in part, a result of roughening of the counter electrode increasing the detectable surface area. The calculation is also strongly dependent on pulse length used in the initial excitation of the Na metal and volume of metal that is excited. Small errors will directly affect the slope of the plot, for example, propagating the largest possible pulse length error results in a 3% error in the m_{NMR} estimate (see discussion in the Supporting Information). Therefore, in the case of continually plated samples, it is reasonable to assume that the NMR is detecting the entire mass of Na metal deposited, indicating that at these current densities electrodeposition of Na on Na metal electrodes results in a large increase in surface volume, which is consistent with a HSA morphology.

Assuming that continuous galvanostatic deposition entirely results in a HSA morphology, we can then interpret the affect of galvanostatic cycling on the accumulation of these microstructures. To compare the influence of cycling on the
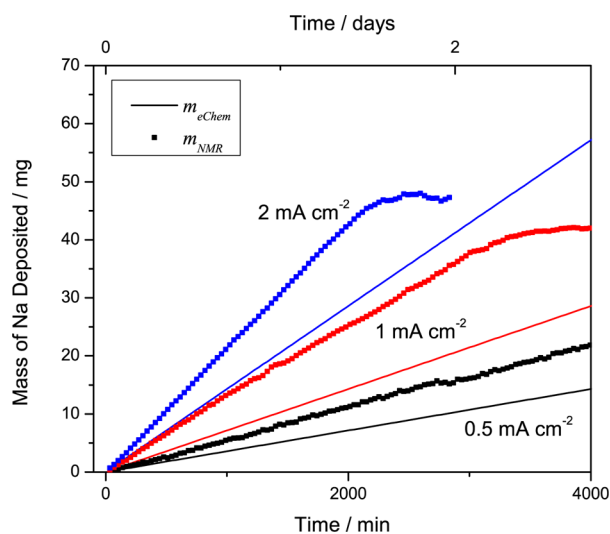

Figure 4. Comparison between the mass of Na deposited electrochemically (m_{eChem}) and that calculated from the NMR spectra (m_{NMR}) for symmetrical Na bag cells continuously galvanostatically plated at various current densities: 2 mA cm^{-2} (blue), 1 mA cm^{-2} (red), and 0.5 mA cm^{-2} (black).

entire data set directly, we define the fraction of high surface area (F_{HSA}) Na metal as the ratio of the mass of deposited Na calculated from the NMR spectra (m_{NMR}) and the total accumulated mass calculated from Faraday's law (m_{eChem}), with the result given in Figure 5.

$$F_{HSA} = \frac{m_{NMR}}{m_{eChem}} \tag{1}$$

In the case of smooth deposition and stripping on both electrodes, NMR would not detect any change in the amount of Na metal (due to the skin depth), and therefore this ratio is zero, close to what is seen for the first cycle at the lowest current studied here (0.5 mA cm^{-2}). In contrast, during the initial stages of cycling, above a current density of 0.5 mA cm^{-2}, all samples exhibit a ratio very close to one, indicating that essentially all the Na is deposited as a HSA deposit, and when the current is reversed, there is very little (or no) removal of these microstructures, the microstructures growing on the opposite electrode. Interestingly, after this initial nucleation-like behavior, the F_{HSA} values at current densities of 1 and 2 mA cm^{-2} plateau to a steady-state value of 0.6. Very different
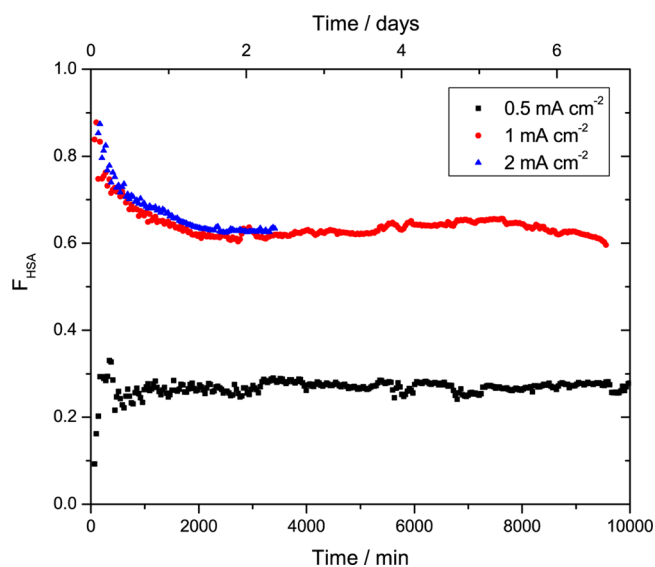
Figure 5. Fraction of high surface area (F_{HSA}) Na during galvanostatic cycling at various current densities. A ratio of 1 indicates completely rough deposition while 0 indicates smooth deposition.

behavior is seen at lower current densities (0.5 mA cm^{-2}), the initial stages of the cycling experiment showing a ratio very close to zero that eventually plateaus to a steady state value of about 0.2. Therefore, the lower current density affords much more efficient removal of the HSA deposits once the electrode is saturated. Regardless of this enhanced efficiency, all current densities investigated in this study cause the continual accumulation of HSA Na metal. F_{HSA} provides a measure of the efficiency of removal of these structures, revealing different behavior at short and longer time periods. We tentatively ascribe this to a transition from a regime where deposition is dominated by the formation of new nucleation sites to a regime where the entire electrode is saturated by the HSA deposits. We explore this proposal in more detail below.

The deposition process can, in principle, be governed by two types of nucleation processes: a progressive or instantaneous nucleation mechanism. In the former, the number of nucleation

sites continues to grow with time, while for instantaneous nucleation, all the nucleation sites are activated simultaneously on the Na metal anode surfaces (i.e., at the onset of deposition). To investigate this further, chronoamperometric experiments (fixed potential, current vs time measurements) were performed to explore the role of the overpotentials (found in the *in situ* cells) on the nature of the nucleation process. The relevant overpotentials for the galvanostatically cycled cells are ∼200, ∼300, and 350 mV (quickly rising to >500 mV) for the current densities 0.5, 1, and 2 mA cm^{-2}, respectively (see Figures S3−S5). A convenient method to analyze the current−time transients measured in the chronoamperometric experiments is the elegant model developed by Scharifker and Hills[27] using nondimensional plots of the transients. The model is derived for 3-dimensional hemispherical nuclei that grow under the influence of a hemispherical (cation) diffusion field, the eventual overlap of the nuclei leading to planar diffusion, allowing application of the Avrami theorem.[27−29] Further supporting details are described in the Supporting Information. This method has been applied to investigate the electrodeposition of a wide variety of metals (such as Li,[30] Zn,[31] and Cu[32]) as well as semiconductors[33] and alloys.[34] In the case of the Li studies, the model was used as the basis to analyze the shape of the nuclei and the influence of electrolyte rather than to investigate the effect of the overpotential. Within this model, the current−time transients are normalized to the maximum current (I_m) and the time at which this occurs (t_m), permitting a nondimensional comparison with their model. Figure 6A−F gives plots of the experimental current−time transients in the form t/t_m vs I^2/I_m^2 alongside the predicted extreme cases of the model (i.e., instantaneous vs progressive nucleation; eqs S17 and S18 in the Supporting Information), allowing a direct comparison with this theory.

An example of the un-normalized current transient is given in the Supporting Information (Figure S7), displaying the characteristic current spike at very short times due to charging of the electrochemical double layer (EDL). In the normalized plots of Figure 6, this results in a high value of I^2/I_m^2 at t/t_m = 0, which drops rapidly with time. Thereafter, the rising current characterizes the nucleation process, in principle, distinguishing
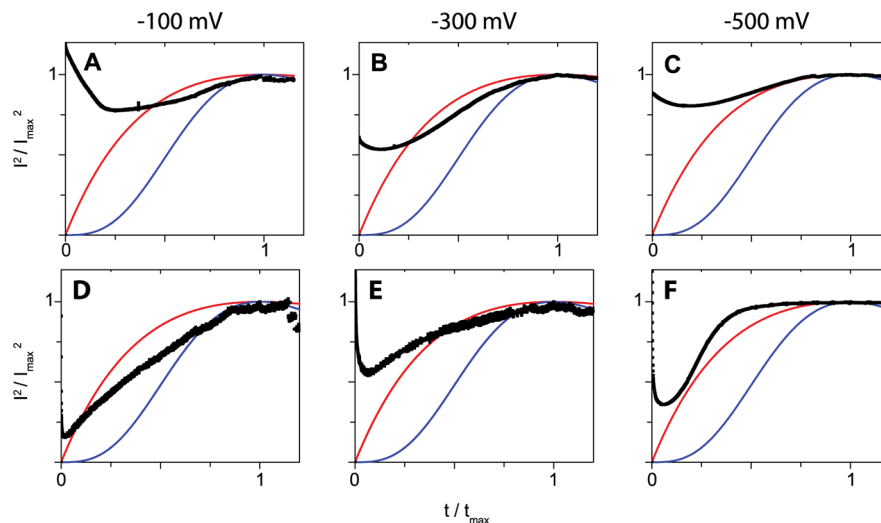
Figure 6. Nondimensional chronoamperograms of 1 M NaTFSI in PC (A−C) and 0.1 M NaTFSI in PC (D−F) at various overpotentials. Scharifker and Hills theoretical models for instantaneous (red) and progressive (blue) nucleation are shown. The data at −100 mV shift toward the progressive regime (blue), suggesting a transition to more progressive nucleation mechanism at an overpotential below −300 mV.

between the cases of a time-dependent and time-independent number of nucleation sites (progressive or instantaneous nucleation, respectively). The experiments shown in Figures 6A−C are, however, convoluted by the influence of the EDL charging and speed of the nucleation process (i.e., the initial high value of I^2/I_m^2 (∼1) due to EDL formation makes it difficult to compare to the predicted initial value of 0, since the Scharifker and Hills model does not account for EDL formation). Nevertheless, the data appear to show a more instantaneous mechanism for an overpotential of −500 mV (Figure 6C), indicated by the current transient never crossing below the plot of the instantaneous model (red curves in Figure 6). To reduce the effect of the initial current spike on the experimental data, a less concentrated electrolyte (0.1 M NaTFSI in PC) was also studied (Figure 6D−F). This has the effect of slowing down the nucleation and growth process to help separate the current rise and maximum from the large EDL charging spike seen for the data in Figure 6A−C. These data lend further support that during the rise of current in the transient there is a transition to more instantaneous nucleation at −300 mV and greater (Figure 6E,F), i.e., as the overpotential increases. At the lower overpotential of −100 mV (Figure 6D), the data clearly cross the instantaneous model (red curves in Figure 6), tending toward the more time-dependent progressive model (blue curves in Figure 6).

Since the current density of the *in situ* NMR cells at 1 mA cm^{-2} and above lead to overpotentials greater than −300 mV (Figure 2 and Supporting Information), the chronoamperometry experiments suggest that the higher current experiments are operating under the conditions of less time-dependent, instantaneous nucleation. The difference between the initial behavior of the galvanostatically cycled 0.5 mA cm^{-2} vs 1 and 2 mA cm^{-2} samples in the NMR experiments and the observed values for the F_{HSA} (Figure 5, at less than 1000 min) can therefore be rationalized as the result of a transition from a more progressive, time-dependent nucleation to an instantaneous one at the higher currents. We suggest that this more progressive nucleation during cycling causes a slower buildup of fewer microstructures over the electrode surface as compared with the rapid saturation caused by current densities of 1 mA cm^{-2} and above, the former being more readily removed on reversing the current.

The Chazalviel model[10] for dendrite formation predicts a time at which the anion concentration adjacent to the electrode falls to zero, causing the development of a space charge layer that promotes dendrite growth. This theory is highly dependent on the diffusivity of charge carriers in the electrolyte and the relative difference between anionic and cationic carriers. A surprisingly high diffusion coefficient for Na$^+$ ion was measured by the pulsed field-gradient NMR (PFG-NMR) method ((1 ± 0.4) × 10^{-9} m^2 s^{-1}) compared to that of the TFSI$^-$ (1.25 × 10^{-10} m^2 s^{-1}) anion in the electrolyte used in this work. Calculation of the critical current density for dendrite formation according to the Chazalviel model,[10] as described in the Supporting Information, indicates an extremely high current density is required for dendrite formation in this system (154 mA cm^{-2}) via this mechanism. Thus, it is clear that we are not working in this regime of dendrite formation and that the dendrite formation we see here is not driven by this mechanism. Indeed, recent studies on Li dendrite formation using magnetic resonance imaging reveals their formation in the nonspace charge regime.[12]

CONCLUSION

For the first time, ^{23}Na *in situ* NMR of Na metal electrodes has been applied and yielded valuable insight into the electrodeposition of Na. Two regimes for the electrochemical deposition of Na on Na metal electrodes, based on current density, are observed. Continuous galvanostatic plating of Na at the current densities studied leads to an entirely HSA morphology. At the higher current densities, the two cycled cells (1 and 2 mA cm^{-2}) exhibit similar behavior in terms of their efficiency in removal of the HSA microstructures. Very different behavior is observed for the lowest current density studied (0.5 mA cm^{-2}), where the efficiency of removal is dramatically increased (and no short-circuiting is observed even after cycling for nearly 8 days). Analysis of the current−time transients performed in a separate experiment highlights that the mechanism of nucleation changes from instantaneous to a more progressive (time dependent) nucleation mechanism at the overpotentials observed for the lower current density of 0.5 mA cm^{-2}. We suggest that this leads to different and fewer microstructures that are more readily removed on cycling. Therefore, these two regimes are distinguished by both the efficiency that HSA deposits can be removed and the time dependence of the nucleation process, both of which are greater at lower current. Unfortunately, despite differences in the nucleation and growth process, both mechanisms yield microstructures that continue to grow as cycling progresses.

ASSOCIATED CONTENT

Ⓢ Supporting Information

The Supporting Information is available free of charge on the ACS Publications website at DOI: 10.1021/jacs.5b12423.

> Details on the NMR quantification, experimental NMR, and electrochemical data and information on the Chazalviel Sand's time and chronoamperometry models (PDF)

AUTHOR INFORMATION

Corresponding Author

*E-mail cpg27@cam.ac.uk (C.P.G.).

Notes

The authors declare no competing financial interest.

REFERENCES

(1) Grosjean, C.; Miranda, P. H.; Perrin, M.; Poggi, P. *Renewable Sustainable Energy Rev.* **2012**, *16*, 1735−1744.

(2) Tarascon, J. M.; Armand, M. *Nature* **2001**, *414*, 359−367.

(3) Aurbach, D.; Zinigrad, E.; Teller, H.; Dan, P. *J. Electrochem. Soc.* **2000**, *147*, 1274−1279.

(4) Bhattacharyya, R.; Key, B.; Chen, H.; Best, A. S.; Hollenkamp, A. F.; Grey, C. P. *Nat. Mater.* **2010**, *9*, 504−510.

(5) Aurbach, D.; Zinigrad, E.; Cohen, Y.; Teller, H. *Solid State Ionics* **2002**, *148*, 405−416.

(6) Eastwood, D. S.; Bayley, P. M.; Chang, H. J.; Taiwo, O. O.; Vila-Comamala, J.; Brett, D. J. L.; Rau, C.; Withers, P. J.; Shearing, P. R.; Grey, C. P.; Lee, P. D. *Chem. Commun. (Cambridge, U. K.)* **2015**, *51*, 266−268.

(7) Barton, J. L.; Bockris, J. O. *Proc. R. Soc. London, Ser. A* **1962**, *268*, 485−505.

(8) Witten, T. A.; Sander, L. M. *Phys. Rev. Lett.* **1981**, *47*, 1400−1403.

(9) Magan, R. V.; Sureshkumar, R.; Lin, B. *J. Phys. Chem. B* **2003**, *107*, 10513−10520.

(10) Chazalviel, J. N. *Phys. Rev. A: At., Mol., Opt. Phys.* **1990**, *42*, 7355−7367.

(11) Brissot, C.; Rosso, M.; Chazalviel, J.-N.; Lascaud, S. *J. Power Sources* **1999**, *81−82*, 925−929.

(12) Chang, H. J.; Ilott, A. J.; Trease, N. M.; Mohammadi, M.; Jerschow, A.; Grey, C. P. *J. Am. Chem. Soc.* **2015**, *137*, 15209−15216.

(13) Yabuuchi, N.; Kubota, K.; Dahbi, M.; Komaba, S. *Chem. Rev.* **2014**, *114*, 11636−11682.

(14) Trease, N. M.; Zhou, L.; Chang, H. J.; Zhu, B. Y.; Grey, C. P. *Solid State Nucl. Magn. Reson.* **2012**, *42*, 62−70.

(15) Wang, H.; Forse, A. C.; Griffin, J. M.; Trease, N. M.; Trognko, L.; Taberna, P.-L.; Simon, P.; Grey, C. P. *J. Am. Chem. Soc.* **2013**, *135*, 18968−18980.

(16) Han, O. H.; Han, K. S.; Shin, C. W.; Lee, J.; Kim, S.-S.; Um, M. S.; Joh, H.-I.; Kim, S.-K.; Ha, H. Y. *Angew. Chem., Int. Ed.* **2012**, *51*, 3842−3845.

(17) Callaghan, P. T. *Translational Dynamics and Magnetic Resonance: Principles of Pulsed Gradient Spin Echo NMR*; Oxford University Press: Oxford, 2011.

(18) Price, W. S.; Chapman, B. E.; Kuchel, P. W. *Bull. Chem. Soc. Jpn.* **1990**, *63*, 2961−2965.

(19) Mishra, B.; Das, L. K.; Sahu, T.; Tripathi, G. S.; Misra, P. K. *Phys. Lett. A* **1984**, *106*, 81−85.

(20) Zhou, L.; Leskes, M.; Ilott, A. J.; Trease, N. M.; Grey, C. P. *J. Magn. Reson.* **2013**, *234*, 44−57.

(21) *CRC Handbook of Chemistry and Physics*, 96th ed.; Haynes, W. M., Ed.; Taylor & Francis: 2015; pp 4−135.

(22) Rosso, M.; Brissot, C.; Teyssot, A.; Dollé, M.; Sannier, L.; Tarascon, J.-M.; Bouchet, R.; Lascaud, S. *Electrochim. Acta* **2006**, *51*, 5334−5340.

(23) Lane, G. H.; Bayley, P. M.; Clare, B. R.; Best, A. S.; MacFarlane, D. R.; Forsyth, M.; Hollenkamp, A. F. *J. Phys. Chem. C* **2010**, *114*, 21775−21785.

(24) Chang, H. J.; Trease, N. M.; Ilott, A. J.; Zeng, D.; Du, L.-S.; Jerschow, A.; Grey, C. P. *J. Phys. Chem. C* **2015**, *119*, 16443−16451.

(25) Ponrouch, A.; Marchante, E.; Courty, M.; Tarascon, J.-M.; Palacín, M. R. *Energy Environ. Sci.* **2012**, *5*, 8572.

(26) Chandrashekar, S.; Trease, N. M.; Chang, H. J.; Du, L.-S.; Grey, C. P.; Jerschow, A. *Nat. Mater.* **2012**, *11*, 311−315.

(27) Scharifker, B.; Hills, G. *Electrochim. Acta* **1983**, *28*, 879−889.

(28) Hills, G. J.; Schiffrin, D. J.; Thompson, J. *Electrochim. Acta* **1974**, *19*, 657−670.

(29) Hills, G. J.; Schiffrin, D. J.; Thompson, J. *Electrochim. Acta* **1974**, *19*, 671−680.

(30) Stark, J. K.; Ding, Y.; Kohl, P. A. *J. Electrochem. Soc.* **2013**, *160*, D337−D342.

(31) Pitner, W. R. *J. Electrochem. Soc.* **1997**, *144*, 3095.

(32) Lin, K. L.; Chen, S. Y.; Mohanty, U. S. *J. Electrochem. Soc.* **2008**, *155*, D251.

(33) Allongue, P.; Souteyrand, E. *J. Electroanal. Chem. Interfacial Electrochem.* **1990**, *286*, 217−237.

(34) Mosby, J. M.; Johnson, D. C.; Prieto, A. L. *J. Electrochem. Soc.* **2010**, *157*, E99.